國立交通大學

光電工程研究所

碩 士 論 文

氧化鋅晶粒大小及氧化鎂鋅之鎂含量對激子-縱模光聲子作用的影響

Effect of ZnO grain size and Mg content of $Mg_xZn_{1-x}O$ on the exciton-longitudinal optical phonon interaction

研 究 生：徐瑋澤

指導教授：謝文峰　教授

中 華 民 國 九 十 七 年 一 月

氧化鋅晶粒大小及氧化鎂鋅之鎂含量對激子-縱模光
聲子作用的影響

Effect of grain size and Mg content of Mg$_x$Zn$_{1-x}$O on the exciton-longitudinal optical phonon interaction

研 究 生：徐瑋澤　　　　　　　　　　Student：Wei-Tse Hsu

指導教授：謝文峰　教授　　　　　　　Advisor：Wen-Feng Hsieh

國 立 交 通 大 學

光電工程研究所

碩 士 論 文

A Thesis
Submitted to Institute of Electro-optical Engineering
College of Electrical Engineering and Computer Science
National Chiao Tung University
in partial Fulfillment of the Requirements
for the Degree of
Master
in
Electro-optical Engineering
January 2007
Hsinchu, Taiwan, Republic of China

中華民國九十七年一月

氧化鋅晶粒大小及氧化鎂鋅之鎂含量對激子-縱模光聲子作用的影響

研究生：徐瑋澤　　　　　　　　　　　　　　指導教授：謝文峰　教授

國立交通大學光電工程研究所

摘要

利用量測由溶膠－凝膠製成不同晶粒大小的氧化鋅及不同鎂含量（$0 \leq x \leq 0.05$）氧化鎂鋅粉末（$Mg_xZn_{1-x}O$）的變溫螢光光譜，可以得到激子－縱模光聲子（LO-phonon）之間耦合的關係。在氧化鋅量子點系統中不明顯激子的縱模光聲子映稱（LO-phonon replicas），以及較小的 13 K 至 300 K 激子能量差顯示激子－縱模光聲子耦合強度的降低。從氧化鋅量子點系統及氧化鎂鋅粉末激子游離能的變大可得知激子波耳半徑的變小。這個結果將導致激子結構極性降低，以致於當氧化鋅量子點縮小及氧化鎂鋅中鎂含量增加，激子－縱模光聲子的交互作用將隨之減弱。

Effect of grain size and Mg content of $Mg_xZn_{1-x}O$ on the exciton-longitudinal optical phonon interaction
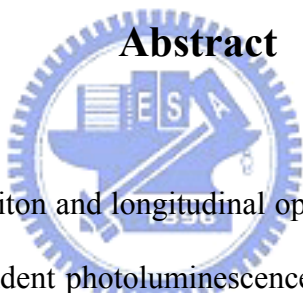
Student: Wei-Tse Hsu   Advisor: Prof. Wen-Fen Hsieh

Institute of Electro-optical Engineering

National Chaio Tung University

Abstract

The coupling between exciton and longitudinal optical (LO) phonon was investigated by using of the temperature-dependent photoluminescence from various sizes of ZnO grain and $Mg_xZn_{1-x}O$ powders in the range of $0 \leq x \leq 0.05$ prepared by sol-gel synthesis. The unapparent LO-phonon replicas of free exciton emission in ZnO quantum dots (QDs) system and the smaller free exciton energy difference between 13 K and 300 K reveal decreasing weighting of exciton–LO phonon coupling strength. From ZnO QDs system and $Mg_xZn_{1-x}O$ powders, the increase of the exciton binding energy resulting from the decrease of the exciton Bohr radius makes the exciton less polar that is responsible for reducing the coupling strength of exciton-LO phonon as shrinking ZnO QDs size and increasing Mg content.

誌謝

　終於要結束求學的生涯啦！一年半的日子，一溜煙的就過去。

　我要感謝我媽還有我的爺爺，這一路來給我經濟、精神上的支持，讓我能一路順利的走到現在，現在我終於可以不再花他們的錢，準備工作賺錢給他們囉！還有依琳，因為妳的幫夫運，讓我能夠進入好的研究所，也能順利的畢業。

　再來要謝謝我的指導教授謝文峰老師，謝謝您不嫌棄我是從動機系來的學生，什麼都不懂，還給了我很多的機會，到最後肯定我，讓我提早畢業，您的肯定讓我對於自己的將來有更足夠的信心去面對所有事。

　國峰學長，我的論文幾乎是你完成的，沒有你每次結結巴巴的把東西教給我，我到現在可能還不知道我在做什麼，沒有你不屑製程的東西，我哪有畢業的東西可以寫。而且畢業前還麻煩你載我東載我西的，讓我瞬間有變實驗室大爺的感覺，真是太感激您了！另外也要感謝金金大學姐，你跟學長一樣幫了我很多忙，讓老師對我有好印象，也讓我copy 了很多你論文的東西，我能夠提早畢業，妳也有很大很大的功勞。

　材料組的學長們，感謝你們過去一年半來在材料實驗上的幫忙，謝謝黃董 Raman方面的指導，松松教我的低溫 PL，小豪陪我調過無數次的光路，以及小郭、維仁的幫忙等等，謝謝你們，也祝福你們以後能順順利利！雷射組的智章、博濟學長，也謝謝你們在實驗室的陪伴，雖然共事機會不多，但還是有請教你們的時候。至賢學長也謝謝你過去一直關心我的身體狀況。

　碩二的夥伴們，我們都要謝謝小賴這個 high 咖讓我們彼此那麼熟，然後小詹的認真

態度也讓我們無形中多學了一些東西，陳厚仁感謝你幫我常常幫我弄電腦（小豪也謝謝你），林易慶要感謝你過去一年來一起分享實驗的心得以及注意的事情，IC 謝謝你幫我們拍了這麼多好照片（小豪也謝謝你），李博士就不用提了，哈哈！

碩一的學弟妹們，由於你們坐裡面，而且又剛過半年，所以跟你們還沒那麼熟，但應該不只我跟你們不熟，所以你們要趕快出來跟學長姊們 social 一下，不然又一眨眼大家都要畢業光了。

還有已故的碩二學長姊們，我可沒忘了提你們一下，尤其現在在奇美逍遙的那位梁飛鴻，感謝當時卡丁車的陪伴，哦對還有棒球。其他學姊們也謝謝你們很照顧我這個學弟。

該謝的都謝完了，沒想到有兩頁這麼多，我們實驗室人太多了，以前的人怎麼一頁就打得完了。

老徐　于　九十七年一月二十九日

iv

Content

List of Figures

Chapter 1 Introduction

1.1 Basic property of ZnO and significance of ZnO related photonic devices

During the last decade, zinc oxide (ZnO) has received much attention because of its wide band gap and large binding energy ($E_b \sim 60$ meV) [1]. Optical and physical properties of semiconductor quantum dots (QDs) have also attracted considerable interests due to their potential applications to light-emitting diodes [2], optically pumped lasers [3] and other electronic devices [4].

1.2 Problem description and Motivation

Although large number of researches on II-VI QDs and III-V QDs have been published [5,6], the properties of ZnO QDs have not been studied as completely as other materials.

To fully utilize ZnO-based technologies, band gap engineering and *p*-type doping are still the remaining issues in modern optoelectronics. Jingbo *et al.* [7] proposed that, using the first-principles band-structure calculations, the *p*-type dopability of ZnO can be improved by lowering the ionization energy of acceptors in ZnO by codoping acceptors with donor or isovalent atoms (e.g., Mg or Be). (Mg,Zn)O alloys have been proved feasible to realize the band gap modulation of ZnO. Additionally, MgZnO can be used as energy barrier layers of ZnO light-emitting devices and ZnO/Mg$_{0.2}$Zn$_{0.8}$O coaxial nanorod single quantum well structures for carrier confinement [8,9]. They are also very promising materials for use as active layers in double heterostructures, e.g., Shibata *et al.* [10] reported Zn$_{1-x}$Mg$_x$O alloys are very brilliant light emitters, even more brilliant than ZnO,

particularly in the high-temperature region. Therefore, it requires a full understanding of material characteristic of MgZnO systems.

The interaction between exciton and longitudinal-optical (LO) phonon has a great influence on the optical properties of polar semiconductors. Ramvall, *et al.* [11] reported a diminishing temperature-dependent shift of the photoluminescence (PL) energy with decreasing GaN QD size caused by a reduction of the LO-phonon coupling. In our previous work [12], the resonant Raman scattering (RRS) of various ZnO QDs sizes reveals that decrease of I_{2LO}/I_{1LO} with decreasing particle sizes gives an evidence for the reduction of exciton-LO phonon interaction with decreasing QDs size. Chang, *et al.* [13] reported that the exciton LO-phonon interaction energy $|E_{ex-ph}|$ theoretically evaluated as functions of electric field strength and the size of the quantum dots. The field enhanced by reducing the separation between electron and hole would increase $|E_{ex-ph}|$; whereas, the decrease of dot size leads to delocalize the wave functions of both electron and hole in turn decreases $|E_{ex-ph}|$. Sun *et al.*, [14] who grew ZnO/ZnMgO multiquantum wells by laser-molecular-beam epitaxy, investigated λ_{Ex-LO} by the temperature dependence of the linewidth of the fundamental excitonic peak from optical absorption spectra. However, the size dependence and Mg concentration of $Mg_xZn_{1-x}O$ powders of exciton-LO-phonon coupling is a complicated problem to be investigated.

1.3 Organization of thesis

In this work, we qualitatively compared the PL spectra of various ZnO particle sizes and Mg-doped ZnO powders with increasing Mg substitution, and quantitatively deduced the weighting of exciton-LO-phonon coupling strength. We finally obtained the reduction of exciton-LO phonon interaction with decreasing ZnO particle sizes and raising Mg substitution in $Mg_xZn_{1-x}O$ powders.

Chapter 2 Theoretical background

2.1 Sol-gel method

An aerosol is a colloidal suspension of particles in a gas (the suspension may be called a fog if the particles are liquid and a smoke if they are solid) and an emulsion is a suspension of liquid droplets in anther liquid.   A sol is a colloidal suspension of solid particles in a liquid, in which the dispersed phase is so small (~1-1000 nm) that gravitational force is negligible and interactions are dominated by the short-range forces, such as Van der Waals attraction and surface charge.   All of these types of colloids can be made by sol-gel synthesis and used to generate polymers or particles from which ceramic materials can be made.   Sol-gel synthesis has two ways to prepare solution.   One way is the metal-organic route with metal alkoxides in organic solvent; the other way is the inorganic route with metal salts in aqueous solution. It is much cheaper and easier to handle metal salts than metal alkoxides, but their reactions are more difficult to control.   The inorganic route is a step of polymerization reactions through hydrolysis and condensation of metal alkoxides $M(OR)^Z$, where M = Si, Ti, Zr, Al, Sn, Ce, and OR is an alkoxy group and Z is the valence or the oxidation state of the metal.   The chemical reactions occur in the inorganic-route sol-gel synthesis including the following steps: First, hydroxylation upon the hydrolysis of alkoxy groups:

$$M - OR + H_2O \rightarrow M - OH + ROH$$

(2.1)

The second step, polycondensation process leads to the formation of branched oligomers and polymers with a metal oxygenation based skeleton and reactive residual hydroxyl and alkoxy groups.   There are 2 competitive mechanisms in the second step:

Oxolation: formation of oxygen bridges involving

$$M - OH + XO - M \rightarrow M - O - M + XOH \ , \tag{2.2}$$
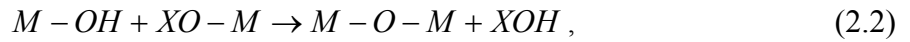
where the hydrolysis ratio ($h = H_2O/M$) decides X=H ($h \gg 2$) or X = R ($h<2$).

Olation: formation of hydroxyl bridges when the coordination of the metallic center is not fully satisfied (N - Z > 0) involving

$$M - OH + HO - M \rightarrow M - (OH)_2 - M \ , \tag{2.3}$$
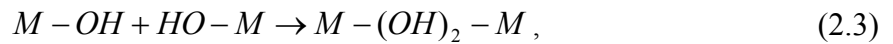
where X = H or R.   The kinetics of olation is usually faster than those of oxolation.   Figure 2-1 presents a schematic of the routes that one could follow within the scope of sol-gel processing [15].   The precursors (starting compounds) for preparation of a colloid consist of a metal or metalloid element surrounded by various ligands.
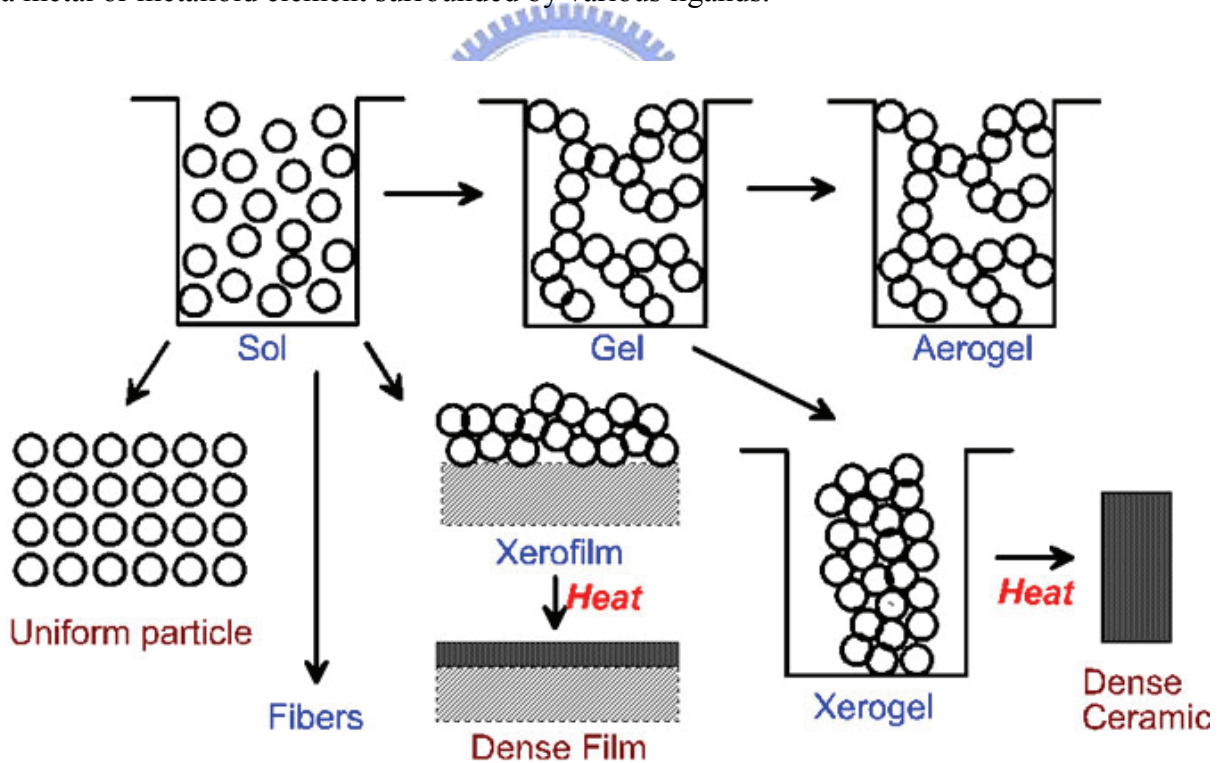
Figure 2-1 Schematic of the routes that one could follow within the scope of sol-gel processing.

2.2 Quantum confinement effect [16]

Recently, it is possible to achieve the low-dimensional structures of materials. Because of reducing dimensional structures, the quantum confinement effects (QCE) become predominant and give rise to a lot of interesting electronic and optical properties. The electron energy will be quantized and varies with dot sizes that cause the variation of band gap energy, binding energy, and Bohr radius.

Two regimes of quantization are usually distinguished in which the crystallite radius R is compared with the exciton Bohr radius or related quantities:

(1) Weak confinement regime for $R \geq a_B$; and

(2) Strong confinement regime for $R < a_B$.
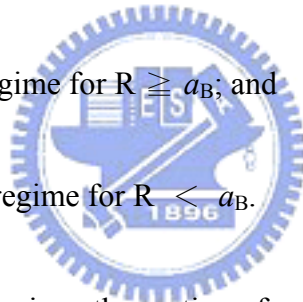
In the weak confinement regime, the motion of center of exciton mass is quantized while the relative motion of electron and hole given by the envelope function $\emptyset(r_e - r_h)$ is hardly affected. In the strong confinement regime, however, the Coulomb energy increases roughly with R^{-1}, and the quantization energy with R^{-2}, so that for sufficiently small values of R one should reach a situation where the Coulomb term can be neglected.

2.2.1 Weak confinement [17]

Coulomb-related correlation between the charged particles handled through the use of a

vary approach involving higher-order wave function of the confined particles, thus, we cannot

neglect the electron hole Coulomb potential. The Schrödinger equation may be written as

$$\left(-\frac{\hbar^2}{2m_e} - \frac{\hbar^2}{2m_h}\right)\nabla^2\Psi + [V_0 + U(r_e - r_h)]\Psi = E_t\Psi. \tag{2.4}$$

Taking $r = r_e - r_h$ and $R = \frac{m_e r_e + m_h r_h}{m_e m_h}$, then the equation becomes

$$\left[-\frac{\hbar^2}{2M}\nabla_R^2 - \frac{\hbar^2}{2\mu}\nabla_r^2 + V(R) + U(r)\right]\Psi = E_t\Psi \tag{2.5}$$

with $M = m_e + m_h$, $\mu = \frac{m_e m_h}{m_e + m_h}$, and E_t as the total energy of the system. If we take

$\Psi = \phi(R)\varphi(r)$ and consider Coulomb interaction first, then we get

$$\left[-\frac{\hbar^2}{2M}\nabla_R^2 + V(R)\right]\phi(R) = E_c\Psi, \tag{2.6}$$

$$\left[-\frac{\hbar^2}{2\mu}\nabla_r^2 + U(r)\right]\varphi(r) = (E_t - E_c)\varphi(r) = E_{ex}\varphi(r). \tag{2.7}$$

Here E_{ex} is resulting from the inclusion of Coulomb interaction. Then we consider the

confinement potential

$$V(R) = 0, R \leq a_B$$

$$V(R) = \infty, R > a_B$$

Thus, the eigenenergy is

$$E_{cn} = \frac{\hbar^2\pi^2 n^2}{2Ma_B^2}, n = 1, 2, 3, \dots \dots \tag{2.8}$$

and the energy of an absorbed resonant photon is

6

$$\hbar\omega_0 = E_t = E_c - E_{ex} = E_g + \frac{\hbar^2\pi^2}{2Ma_B^2} - E_{ex}$$

$$\hbar\omega_0 = E_g + \frac{\hbar^2\pi^2}{2Ma_B^2} - \frac{1.8e^2}{4\pi\varepsilon\varepsilon_0 R} \qquad (2.9)$$

where E_g is band gap energy.

2.2.2 Strong confinement

The size quantization band states of the electron and hole is dominated by the kinetic

energies of electron and hole which are larger than the electron-hole Coulomb potential,

therefore, the effect of the Coulomb attraction between the electron and hole can be treated as

a perturbation.   The Schrödinger equation can be written as

$$\left(-\frac{\hbar^2}{2m_e} - \frac{\hbar^2}{2m_h}\right)\nabla^2\Psi + V_0\Psi = E\Psi \qquad (2.10)$$

Again, the confinement potential is defined as

$$V(r) = 0, r \le a_B,$$

$$V(r) = \infty, r > a_B,$$

and the energy of electron or hole is

$$E_{cn} = \frac{\hbar^2\pi^2 n^2}{2m_{e,h}a_B^2}, n = 1,2,3,\dots\dots \qquad (2.11)$$
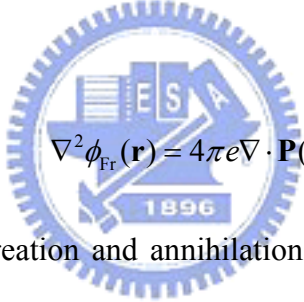
The energy of an absorbed resonant photon is

$$\hbar\omega_0 = E_g + \frac{\hbar^2\pi^2}{2a_B^2}\left(\frac{1}{m_e} + \frac{1}{m_h}\right) = E_g + \frac{\hbar^2\pi^2}{2\mu a_B^2} \qquad (2.12)$$

with $\mu = \frac{m_e m_h}{m_e + m_h}$ as the reduced mass of electron and hole.

2.3 Fröhlich interaction [18]

One of the most important carrier-phonon scattering mechanisms in semiconductors occurs when charge carriers interact with the electric polarization, **P(r)**, produced by the relative displacement of positive and negative ions. In low-defect polar semiconductors such as GaAs, InP, and GaN, carrier scattering in polar semiconductors at RT is dominated by this polar-optical-phonon (POP) scattering mechanism. The POP-carrier interaction is referred to as the Fröhlich interaction. Here, the potential energy associated with the Fröhlich interaction will be denoted by $\phi_{Fr}(\mathbf{r})$. The polarization **P** associated with polar-optical phonons and the potential energy associated with the Fröhlich interaction, $\phi_{Fr}(\mathbf{r})$, are related by

$$\nabla^2 \phi_{Fr}(\mathbf{r}) = 4\pi e \nabla \cdot \mathbf{P}(\mathbf{r}).$$ (2.13)

In terms of the phonon creation and annihilation operators, the operators act on states each having a given number of phonons. The creation operator acting on a state of n_q phonons of wavevector q increases the number of phonons to $n_q + 1$ and the phonon annihilation operator acting on a state of n_q phonons of wavevector q decreases the number of phonons to $n_q - 1$. **P(r)** may be written as

$$\mathbf{P}(\mathbf{r}) = \zeta \sum_{j=1,2,3} \int \frac{d^3\mathbf{q}}{(2\pi)^3} (a_\mathbf{q} e^{i\mathbf{q}\cdot\mathbf{r}} \mathbf{e}_{\mathbf{q},j} + a_\mathbf{q}^+ e^{-i\mathbf{q}\cdot\mathbf{r}} \mathbf{e}_{\mathbf{q},j}^*),$$ (2.14)

where $\mathbf{e}_{\mathbf{q},j}$ represents the polarization vector associated with **P(r)** and **q** is the phonon wavevector; then, it follows that

$$4\pi\nabla\cdot\mathbf{P}(\mathbf{r}) = 4\pi i\zeta \sum_{j=1,2,3} \int \frac{d^3\mathbf{q}}{(2\pi)^3} (a_\mathbf{q} e^{i\mathbf{q}\cdot\mathbf{r}} \mathbf{q}\cdot\mathbf{e}_{\mathbf{q},j} - a_\mathbf{q}^+ e^{-i\mathbf{q}\cdot\mathbf{r}} \mathbf{q}\cdot\mathbf{e}_{\mathbf{q},j}^*). \qquad (2.15)$$

Consider the case of a polar crystal with two atoms per unit cell, such as GaAs. The dominant contribution to $\mathbf{P}(\mathbf{r})$ results from the phonon modes in which the normal distance between the planes of positive and negative charge varies. Such modes are obviously the longitudinal optical (LO) modes since in the case of LO modes $\mathbf{e}_{\mathbf{q},j}$ is parallel to $\mathbf{q}$. However, transverse optical (TO) phonons produce displacements of the planes of charge such that they remain at fixed distances from each other; that is, the charge planes slide by each other but the normal distance between planes of opposite charge does not change. So, TO modes make negligible contributions to $\mathbf{P}(\mathbf{r})$. For TO phonons, $\mathbf{e}_{\mathbf{q},j}\cdot\mathbf{q} = 0$. Accordingly,

$$4\pi\nabla\cdot\mathbf{P}(\mathbf{r}) = 4\pi i\zeta \int \frac{d^3\mathbf{q}}{(2\pi)^3} (a_\mathbf{q} e^{i\mathbf{q}\cdot\mathbf{r}} q - a_\mathbf{q}^+ e^{-i\mathbf{q}\cdot\mathbf{r}} q), \qquad (2.16)$$

and the potential energy associated with the Fröhlich interaction, $\phi_{Fr}(\mathbf{r})$, is given by

$$H_{Fr} = \phi_{Fr}(\mathbf{r}) = -4\pi i e\zeta \int \frac{d^3\mathbf{q}}{(2\pi)^3} \frac{1}{q} (a_\mathbf{q} e^{i\mathbf{q}\cdot\mathbf{r}} - a_\mathbf{q}^+ e^{-i\mathbf{q}\cdot\mathbf{r}}), \qquad (2.17)$$

where $\phi_{Fr}(\mathbf{r})$, has been denoted by H_{Fr}, the Fröhlich interaction Hamiltonian since $\phi_{Fr}(\mathbf{r})$ is the only term contribution to it. The dependence of $\phi_{Fr}(\mathbf{r})$ on q^{-1} is familiar from the Coulomb interaction; the coupling constant ζ remains to be determined.

In polar semiconductors, the masses m and M carry opposite charges, e^*, as a result of the redistribution of the charge associated with polar bonding. The electric polarization $\mathbf{P}(\mathbf{r})$ may be written as

$$\mathbf{P(r)} = \frac{Ne^*}{\varepsilon(\infty)}\mathbf{u_q(r)}$$

$$= \frac{Ne^*}{\varepsilon(\infty)}\frac{1}{\sqrt{N}}\sum_q \sum_{j=1,2,3}\sqrt{\frac{\hbar}{2(\frac{mM}{m+M})\omega_{LO}}}\times(a_\mathbf{q}e^{i\mathbf{q}\cdot\mathbf{r}}\mathbf{e}_{\mathbf{q},j}-a_\mathbf{q}^+e^{-i\mathbf{q}\cdot\mathbf{r}}\mathbf{e}_{\mathbf{q},j}^*),$$

(2.18)

where the division by $\varepsilon(\infty)$ accounts for screening, the normal-mode phonon displacement has been used for $\mathbf{u(r)}$, q is summed over all wavevectors in the Brillouin zone, and N is the number of unit cells in the sample.   By noticing that

$$\frac{1}{\sqrt{V}}\sum_q \leftrightarrow \int\frac{d^3\mathbf{q}}{(2\pi)^3}$$

(2.19)

and by comparing expressions (2.14) and (2.18), it follows that

$$\zeta = \frac{Ne^*}{\varepsilon(\infty)}\frac{1}{\sqrt{N}}\sqrt{\frac{\hbar}{2(\frac{mM}{m+M})\omega_{LO}}}.$$

(2.20)

However, from the dielectric constant due to the electronic response

$$\varepsilon(\omega) = \varepsilon(\infty) + \frac{4\pi}{(\omega_{TO}^2 - \omega^2)}\frac{Ne^{*2}}{\varepsilon(\infty)}(\frac{1}{m}+\frac{1}{M})$$ evaluated for $\omega = \omega_0$, it follows that

$$\frac{Ne^{*2}}{\varepsilon(\infty)^2}(\frac{1}{m}+\frac{1}{M}) = \frac{\omega_{LO}^2 - \omega_{TO}^2}{4\pi\varepsilon(\infty)}$$

$$= \frac{\omega_{LO}^2}{4\pi}[\frac{1}{\varepsilon(\infty)}-\frac{1}{\varepsilon(\infty)}\frac{\omega_{TO}^2}{\omega_{LO}^2}]$$

$$= \frac{\omega_{LO}^2}{4\pi}[\frac{1}{\varepsilon(\infty)}-\frac{1}{\varepsilon(0)}],$$

(2.21)

so that

$$\zeta = \frac{Ne^*}{\varepsilon(\infty)} \frac{1}{\sqrt{N}} \sqrt{\frac{\hbar}{2(\frac{mM}{m+M})\omega_{LO}}} = \sqrt{\frac{\hbar}{2\omega_{LO}} \frac{\omega_{LO}^2}{4\pi} [\frac{1}{\varepsilon(\infty)} - \frac{1}{\varepsilon(0)}]} \; ,$$

(2.22)

and

$$H_{Fr} = \phi_{Fr}(\mathbf{r}) = -4\pi i e \zeta \int \frac{d^3\mathbf{q}}{(2\pi)^3} \frac{1}{q} (a_{\mathbf{q}} e^{i\mathbf{q}.\mathbf{r}} - a_{\mathbf{q}}^+ e^{-i\mathbf{q}.\mathbf{r}})$$

$$= -i \sqrt{\frac{2\pi e^2 \hbar \omega_{LO}}{V} [\frac{1}{\varepsilon(\infty)} - \frac{1}{\varepsilon(0)}]} \sum_q \frac{1}{q} (a_{\mathbf{q}} e^{i\mathbf{q}.\mathbf{r}} - a_{\mathbf{q}}^+ e^{-i\mathbf{q}.\mathbf{r}}) \; .$$

(2.23)

Besides, the lattice distortion created by a phonon resulting in a local change in the crystal's energy band; the energy associated with the change is known as the deformation potential and it represents one of the major scattering mechanisms in non-polar semiconductors. Indeed, the deformation-potential interaction is a dominant source of electron energy loss in silicon-based electronic devices. The piezoelectric interaction occurs in all polar crystals lacking inversion symmetry. In the general case, the application of an external strain to a piezoelectric crystal will produce a macroscopic polarization as a result of the displacements of ions. Thus an acoustic phonon mode will drive a macroscopic polarization in a piezoelectric crystal.

2.4 Photoluminescence characterization [19]

2.4.1 General concepts

The ground state of the electronic system of a perfect semiconductor is a completely filled valance band and a completely empty conduction band. We can define this state as the "zero" energy or "vacuum" state. If we start from the ground state and excite one electron to the conduction band, we simultaneously create a hole in the valance band. In this sense an optical excitation is a two-particle transition. The same is true for the recombination process. An electron in the conduction band can return radiatively or nonradiatively into the valance band only if there is a free space, i.e., a hole. Two quasi-particles are annihilated in the recombination process. What we need for the understanding of the optical properties of the electronic system of a semiconductor is therefore a description of the excited states of the N-particle problem. The quanta of these excitations are called excitons. Here we will consider the so-called *Wannier excitons* more specifically. In Wannier excitons, the Bohr radius (i.e. the mean distance between electron and hole) is larger compared to the lattice constant. This situation is well realized in narrow-gap semiconductors which have large ε ($\gg 1$) and small μ ($\ll m_0$).

Using the effective mass approximation, the Coulomb interaction between electron and hole leads to a hydrogen-like problem with a Coulomb potential term $\dfrac{-e^2}{4\pi\varepsilon_0\varepsilon\left|r_e - r_h\right|}$.

Indeed excitons in semiconductors form, to a good approximation, a hydrogen or positronium like series of states below the gap. For a simple parabolic band in a direct-gap semiconductor one can separate the relative motion of electron and hole and the motion of the center of mass. This leads to the dispersion relation of exciton as shown in Fig. 2-2

$$E_{ex}(n_{B}, \boldsymbol{K}) = E_{g} - Ry^{*}\frac{1}{n_{B}^{2}} + \frac{\hbar^{2}\boldsymbol{K}^{2}}{2M} \qquad (2.24)$$

where n_B = 1, 2, 3… is the principal quantum number, $Ry^{*} = 13.6\text{eV}\frac{\mu}{m_{0}}\frac{1}{\varepsilon^{2}}$ is the exciton

binding energy, $M = m_{e} + m_{h}$, and $\boldsymbol{K} = \boldsymbol{k}_{e} + \boldsymbol{k}_{h}$ are the translational mass and wave vector of

the exciton, respectively. The series of exciton states in (2.24) has an effective Rydberg

energy Ry^{*} modified by the reduced mass of electron and hole and the dielectric constant of

the medium in which these particles move. The radius of the exciton equals the Bohr radius

of the H atom again modified by ε and μ. Using the material parameters for typical

semiconductors one finds that the orbits of electron and hole around their common center of

mass average over many unit cells and this in turn justifies the effective mass approximation

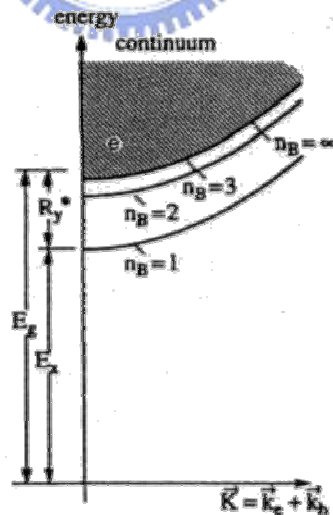in a self-consistent way. Theses excitons are called Wannier excitons.

Fig. 2-2 A pair excitation in the scheme of valence and conduction band in the exciton picture for a direct gap

semiconductor. [16]

2.4.2 Exciton-related emission [20]

Exciton photoluminescence (PL) is very sensitive to the quality of crystal structures and to the presence of defects. Therefore, the regularities of the change in exciton spectra as a function of composition and structural peculiarities enable one to use them to control the quality of the crystal optically. Impurities and their associations, main lattice defects and their impurity associations, and exciton and exciton impurity complexes all play an important role in the luminescence, which significantly complicates the observation of free-exciton PL. Generally, PL spectrum of single crystal ZnO consists mainly of two bands. The one in UV region corresponds to near-band-edge (NBE) emission is attributed to exciton states; the other one in visible region is due to structural defects and impurities.
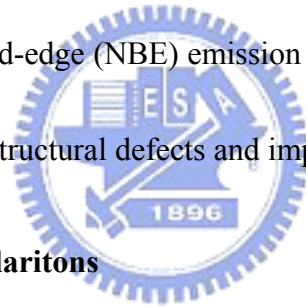
2.4.3.1 Free excitons and polaritons

The optical properties of a semiconductor are connected with both intrinsic and extrinsic effects. For a start, the intrinsic excitonic features in the 3.376–3.450 eV range are discussed. The wurtzite ZnO conduction band is mainly constructed from the s-like state having (Γ_7^c) symmetry, whereas the valence band is a p-like state, which is split into three bands due to the influence of crystal field and spin-orbit interactions. The ordering of the crystal-field and spin-orbit coupling split states of the valence-band maximum in wurtzite ZnO was calculated by our group using tight-binding theory. The obtained electronic band structure of wurtzite ZnO is shown in Fig. 2-3. The valence-band symmetry ordering (A-Γ_9, B-Γ_7, and C-Γ_7) in ZnO is the same as that observed in low temperature PL and magneto-luminescence

measurements by other researchers.
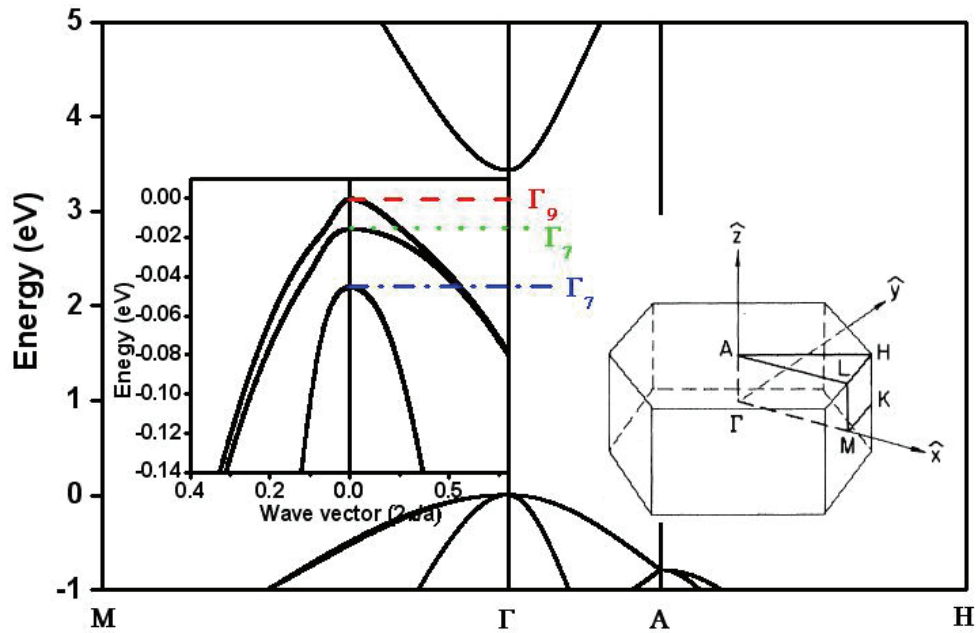
Fig. 2-3 The electronic band structure of wurtzite ZnO.   [unpublished]

Group theoretical arguments and the direct product of the group representations of the band symmetries (Γ_7 for the conduction band, Γ_9 for the A valence band, upper Γ_7 for the B valence band, and lower Γ_7 for the C valence band) will result in the following intrinsic exciton ground state symmetries:

$$\Gamma_7 \times \Gamma_9 \to \Gamma_5 + \Gamma_6 , \quad \Gamma_7 \times \Gamma_7 \to \Gamma_5 + \Gamma_1 + \Gamma_2$$

The Γ_5 and Γ_6 exciton ground states are both doubly degenerate, whereas Γ_1 and Γ_2 are both singly degenerate. Γ_5 and Γ_1 are allowed transitions with $\mathbf{E} \perp \mathbf{c}$ and $\mathbf{E} \parallel \mathbf{c}$, respectively, but the Γ_6 and Γ_2 are not allowed.
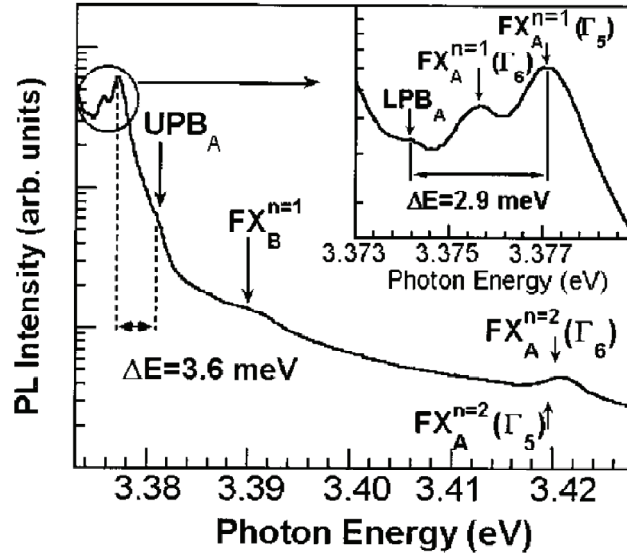
Fig. 2-4 Free excitonic fine structure region of the 10 K PL spectrum for the ZnO single crystal.

Figure 2-4 displays the PL spectrum in the range of fundamental excitonic region measured at 10 K in the $\mathbf{E} \perp \mathbf{c}$ polarization geometry for a high quality ZnO crystal. A-free exciton and its first excited state emission are observed at $FX_A^{n=1} = 3.3771$ eV (3.3757 eV for Γ_6) and $FX_A^{n=2} = 3.4220$ eV for Γ_5 (3.4202 eV for Γ_6) band symmetry, respectively. Although, at $k = 0$, Γ_6 exciton is forbidden in the current measurement mode of polarization, it is still observed, due to the fact that the photon has finite momentum. Geometrical effects such as not having the sample orientation exactly perpendicular to the electric field can also be a reason for the observed Γ_6 transition. Using the energy separation of ground state and excited state, the exciton binding energy and band gap energy can be evaluated. The energy difference of about 45 meV gives A-free exciton binding energy of 60 meV and a

corresponding band gap energy of 3.4371 eV at 10 K. Based on the reported energy

separation of the A- and B-free excitons (in the range of 9–15 meV), we assigned the weak

emission centered at 3.3898 eV, which is about 12.7 meV apart from the A exciton to the B

exciton transition.

Additional fine structure of exciton lines was also observed in low temperature PL

spectra.   In strongly polar materials like ZnO transverse Γ_5 excitons couple with photons to

form polaritons.   Therefore, as indicated in Fig. 2-4, the $FX_A^{n=1}(\Gamma_5)$ exciton line has two

components.   The higher energy component at 3.3810 eV, which is 3.6 meV apart from the

A exciton, can be assigned to the so-called longitudinal exciton (upper polariton

branch—UPB$_A$).   The lower energy component at 3.3742 eV, which is about 2.9 meV apart

from the A exciton, corresponds to the recombination from the "bottleneck" region, in which

the photon and free-exciton dispersion curves cross (lower polariton branch—LPB$_A$).   As a

result, their dispersion curves are illustrated in Figure 2-5.   We will explain the energy

diagram of a system consisting of a crystal and radiation below.   Since Γ_6 excitons do not

have transverse character, they do not interact with light to form polaritons, and thus have

only normal free-exciton dispersion curves as seen in the PL spectra.

The incident radiation in the exciton band region is converted to the exciton polariton

inside the crystal and it has two modes, the upper and lower branches.   The energy of the

polariton is shown in Fig. 2-5 as a function of wave vector *k*.   The broken line represents the

relation between the energy and wave vector of the photon in vacuum.   The absorption of a

photon creates an upper-branch polariton at *a,* which is then scattered to state *b* of the

lower-branch polariton.   The polariton thus formed is thermalized from *b* to *c* through

phonon and point-defect scattering.   The thermalized polariton can be annihilated as a

photon at *d* (direct radiative annihilation) or move in the crystal to be ionized or annihilated

nonradiatively at imperfections, since the thermalized state has a longer lifetime.   If the

incident radiation energy is below the bottom of the upper-branch polariton, it generates the
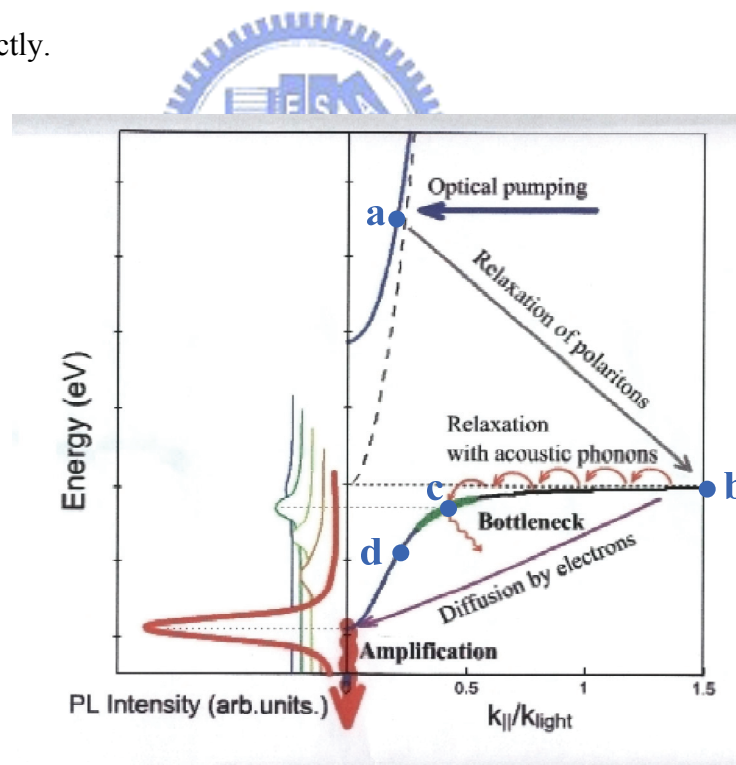
lower polariton directly.

Fig. 2-5 Dispersion curves of exciton and exciton polaritons.

Here two assumptions are necessary. First, most inelastic scattering is caused by the LO phonon. Second, the probability for a thermalized exciton to be ionized or annihilated at imperfections is larger than that for it to be annihilated as a photon at d after being scattered from b to c. Under these assumptions if the energy difference between the upper polariton state a and the lower polariton state d is an integral multiple of the LO phonon energy, the cascade scattering of the polariton into state d occurs very efficiently and it is annihilated as a photon. If this energy difference is not an integral multiple of the phonon energy, the polariton is scattered and thermalized in the state near c in the lower-branch polariton and then it is ionized or trapped at imperfections before reaching state d. Thus the LO phonon structure is expected in the excitation spectrum of the free-exciton emission.
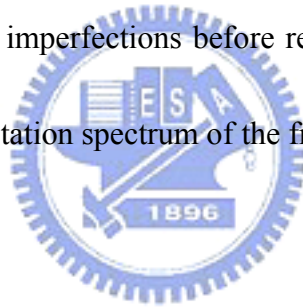
2.4.3.2　LO-phonon replicas

As indicated in Fig. 2-6, the bump at the higher energy side of the spectrum labeled as 1LO (FX_A) has a peak around 3.306 eV, which is the expected value for the 1LO-phonon replica of the free exciton peak (about 71 meV apart from the $FX_A^{n=1}$ free-exciton peak).

Although weak, the second and the third order LO phonon replicas labeled as 2LO (FX_A) and 3LO (FX_A) are also observed in the PL spectrum. It should be noted that LO-phonon replicas occur with a separation of 71–73 meV, which corresponds to the LO-phonon energy

in ZnO.   The peak at 3.2898 eV is the first LO-phonon replica of both 3.3618 and 3.3605 eV

lines, whereas the first LO-phonon replica of 3.3650 eV line is seen as a shoulder on the

high-energy side of this intense peak.
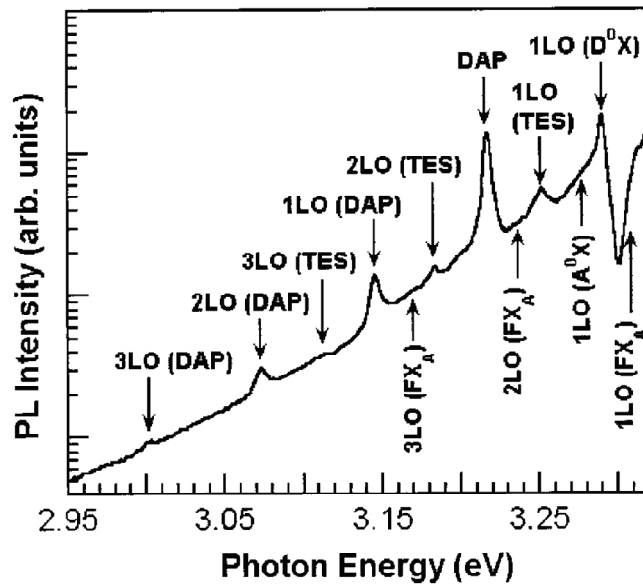
Fig. 2-6 10 K PL spectrum in the region where LO-Phonon replicas are expected to appear.

2.4.3 The information obtained from PL spectrum

The temperature dependence of the PL spectrum, intensity and energy of free exciton in

particular have been used to obtain information about electronic gap levels in various

semiconductors.   Below we will discuss two methods to obtain the binding energy and the

relation of exciton-phonon coupling.

2.4.3.1 Binding energy [21]

It is recognized that a host of different processes contribute to the reduction of the PL intensity as temperature increases. In CdTe, thermal release of trapped carriers, followed by capture in a nonradiative recombination center, is proposed as the principal mechanism of thermal quenching. In some cases the thermal quench is pictured as being essentially due to a transition from the excited state directly to the ground state via the so-called internal mechanism.

Irrespective of the specific quenching mechanism, the temperature dependence of the integrated intensity $I(T)$ of PL bands is most often described by the expression

$$I(T) = \frac{I_0}{1 + \alpha \exp\left(-\frac{E_a}{kT}\right)} \tag{2.25}$$

with the process rate parameter α and activation energy E_a. If the expression treats for higher temperature region (T > 60 K), and then the E_a is the binding energy of free exciton.

2.4.3.2 Band gap energy variation with temperature [22]

Both mechanisms have the contributions to the variation of band gap energy $E(T)$: exciton-phonon interaction and the thermal lattice expansion. The contributions of the individual lattice oscillators with energies $\varepsilon = \hbar\omega$ are proportional to the average phonon

occupation number, $\bar{n} = [\exp(\varepsilon/k_B T) - 1]^{-1}$.   Therefore, *E(T)* can be represented as

$$E(T) = E(0) - \frac{\alpha}{k_B} \int d\varepsilon \frac{\varepsilon \, w(\varepsilon)}{\exp(\epsilon/k_B T) - 1}.$$ (2.26)

Here $\alpha = -dE(T)/dT|_{T \to \infty}$ is the slope of the linear *T* dependence in the high temperature limit, and $w(\varepsilon) \geq 0$ is the normalized weighting function of the phonon oscillators, $\int d\varepsilon \, \varepsilon \, w(\varepsilon) = 1$.

A convenient analytical treatment of *E(T)* is obtained: we reduced the integration term to a summation term

$$E(T) = E(0) - \sum_i \frac{\alpha_{0i}}{\exp(\epsilon_i/k_B T) - 1},$$ (2.27)

each term represents a phonon mode to the particular material. α_{0i} represents the weighting of certain phonon mode.   Therefore, we can obtain the contribution of certain phonon mode by deducing the weighting α_{0i}.

Chapter 3 Experimental procedures

3.1 Sample preparation

3.1.1 ZnO quantum dots synthesized by varying concentration of zinc precursor

ZnO quantum dots were synthesized by the sol-gel synthesis as the following procedure. Stoichiometric zinc acetate dihydrate [99.5% $Zn(OAc)_2 \cdot 2H_2O$, Riedel-deHaen] was dissolved into diethylene glycol [99.5% DEG, ethylenediamine-tetra-acetic acid (EDTA)] to make 0.1 M, 0.05 M, 0.01 M solutions. The resultant solutions were put separately in a centrifuge operating at 3000 rpm for 30 minutes, and transparent solutions were obtained containing dispersed single crystalline ZnO nanocrystals. Next, the solutions were dropped onto Si (100) substrates and dried at 150°C for further characterization.
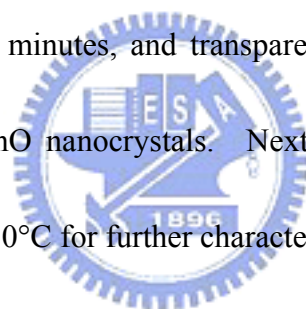
3.1.2 $Mg_xZn_{1-x}O$ powders synthesized by varying molar ratio of Mg/Zn

$Mg_xZn_{1-x}O$ powders were synthesized using the aqueous sol prepared by stoichiometric zinc acetate dihydrate [99.5% $Zn(OAc)_2 \cdot 2H_2O$, Riedel-deHaen] and magnesium acetate tetrahydrate [99.5% $Mg(OAc)_2 \cdot 4H_2O$, Riedel-deHaen] (Mg/Zn = 0, 3, and 5% in molar ratio) dissolved into methanol. The sol was dried in a furnace at 900°C under air atmosphere for 1 hour, and then slowly cooled to room temperature.

3.2   Photoluminescence system

For photoluminescence (PL) measurement, we used a He–Cd laser ($\lambda = 325$ nm) as the

excitation source.   The schematic of the PL system is shown in Fig 3-1.   The excitation

laser beam was directed normally and focused onto the sample surface with power being

varied with a variable optical attenuator.   The spot size on the sample is about 100 μm.

Spontaneous and stimulated emissions were collected by a fiber bundle and coupled into a

0.32 cm focal-length monochromator (TRIAX 320) with a 1200 lines/mm grating, then

detected by either an electrically cooled CCD (CCD-3000) or a photomultiplier tube

(PMT-HVPS) detector.   The temperature-dependent PL measurements were carried out using

a closed cycle cryogenic system.   A closed cycle refrigerator was used to set the temperature
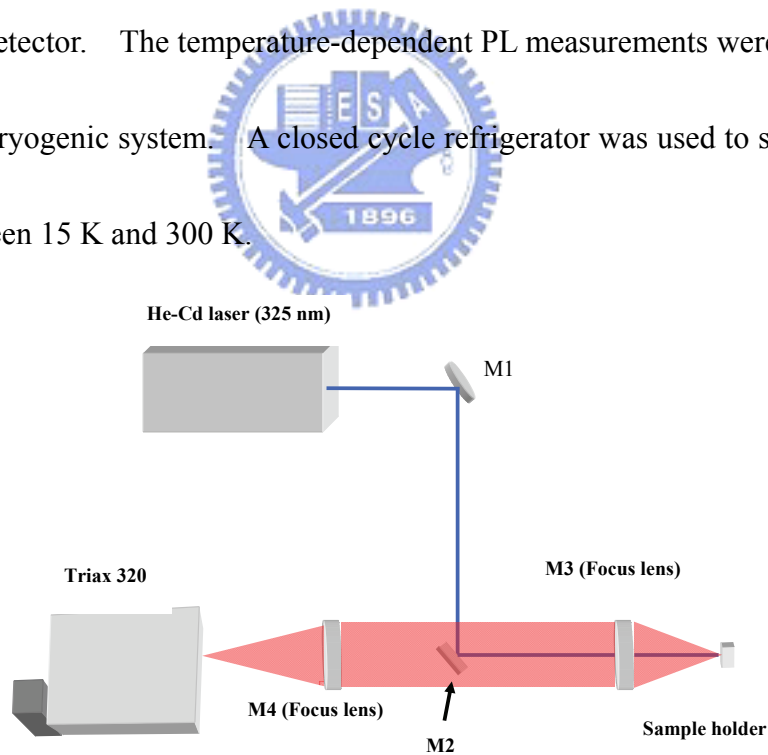
anywhere between 15 K and 300 K.

Figure 3-1 PL detection system.

Chapter 4 Results and discussion

4.1 ZnO quantum dots system

4.1.1 Photoluminescence spectra of different sizes of ZnO particles

Figure 4-1 shows the PL spectra of different ZnO sizes at 13 K. The spectra of ZnO powders consists of the free exaction emission ($FX_A^{n=1}$) and the donor-bound exciton (D^0X) emission peaks along with three obvious LO-phonon replicas [23]. The $FX_A^{n=1}$ emission of ZnO powders is 3.377eV which behaves as ZnO bulk. The energy shift (dash line) from 3.377 eV to 3.475 eV due to quantum confinement effect (QCE) can be observed. The full width at half maximum which increases as the dot size decreases may be caused by the contribution of surface-optical phonon [24], surface-bound acceptor exciton complexes [25], and size distribution. Accordingly, we observed that LO-phonon replicas are obvious in ZnO powders but are unapparent in other QD-samples. Duke *et al.* interpreted the intensities of LO-phonon replicas depend strongly on their exciton-phonon coupling strengths [26]. This result reveals reducing exciton-phonon coupling as decreasing the particle sizes that is consistent with our previous report [12].
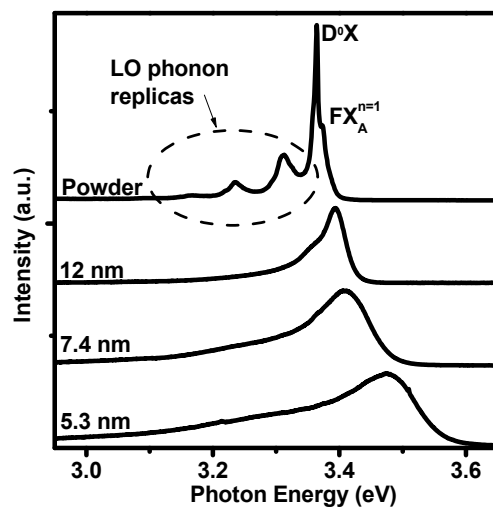

Figure 4-1 PL spectra of different ZnO particle sizes at 13K.

4.1.2 Temperature-dependent PL of different sizes of ZnO particles

Figure 4-2 displays the temperature-dependent PL of different sizes of ZnO, it reveals only single one band for T = 13 ~ 260 K in QDs system. Due to small binding energy of D^0X, it will be ionized as T > 100 K, so we can easily attribute the single band to the $FX_A^{n=1}$ emission. We also find that the peak energy difference of $FX_A^{n=1}$ in QDs system between 13 K and 260 K are ~ 44, 18 and 15 meV that are smaller than 65 meV of ZnO powders. It is known that the main contribution to the energy shift is the Fröhlich interaction [27], a result of Coulomb interaction. We will do further analysis on this matter in the following section.
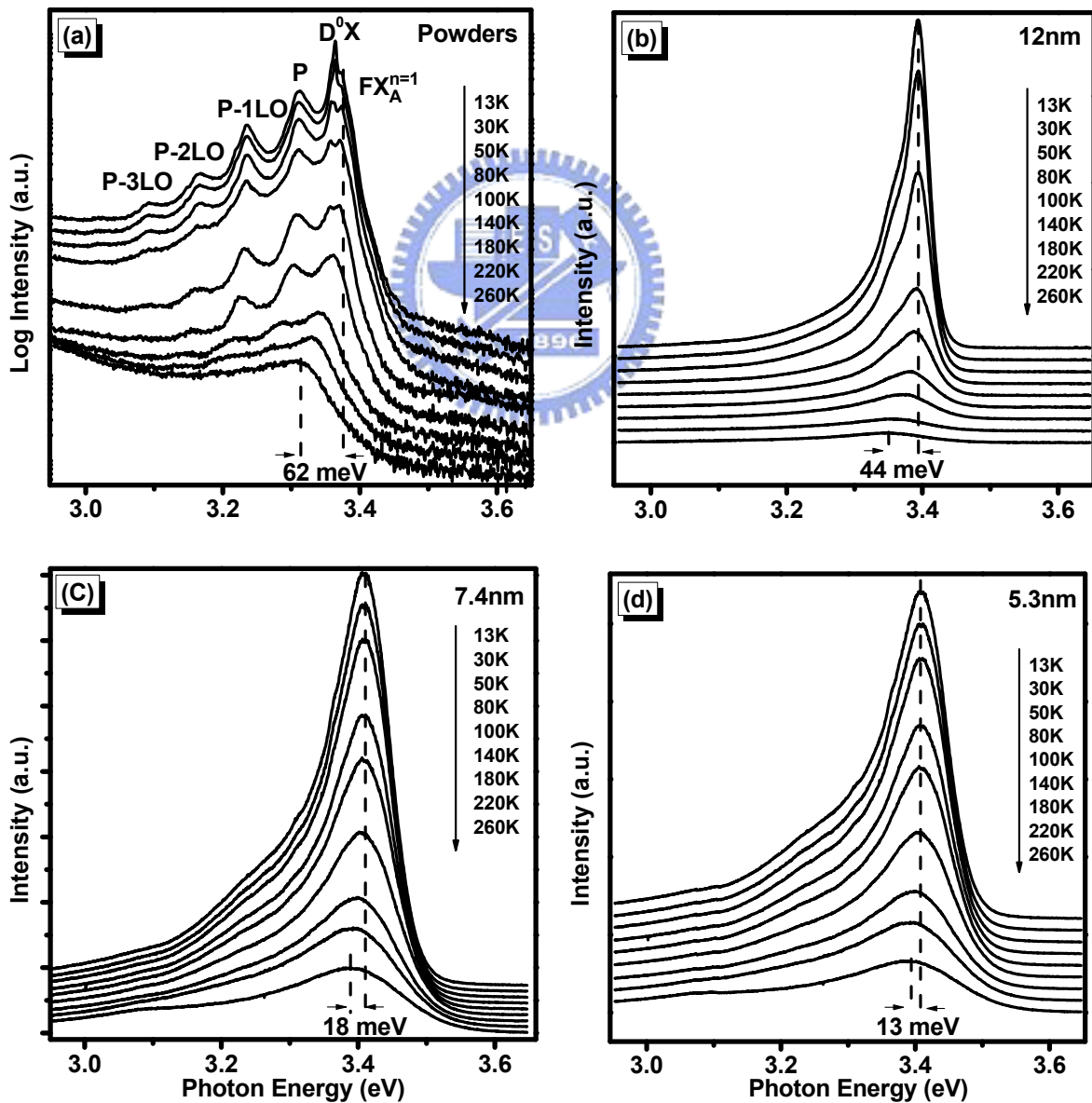

Figure 4-2 Temperature-dependence PL spectra of (a) Powders, (b) 12nm, (c) 7.4 nm, (d) 5.3 nm.

4.1.3 The weighting of exciton-LO phonon coupling strength (α_0)

In order to quantitatively investigate the relation between the quantum confinement size and the exciton-LO phonon interaction, we adopted the formula (2.27). As our previous RRS [12] and PL results, the most promising LO-phonon involvement in RRS and PL is the one having energy of 71 to 72 meV corresponding to the A1(LO) phonon. We therefore take only a single one of the summation terms of Eq. (2.27) with $\hbar\omega$ = 72 meV into account to discuss the exciton-LO phonon coupling and α_0 represents the weighting of exciton-A1(LO) phonon coupling. Although the LO-phonon energy depends on the size of QD, from our fitting result even for 5.3 nm QD, the phonon energy shift is less than 1 meV, it is insufficient (< 4%) to change α_0. We plotted the fitting results α_0 = 0.59, 0.40, 0.21, and 0.19 for powders, 12 nm, 7.4 nm, and 5.3 nm QDs, respectively in Fig. 4-3. These results are consistent with the observations of PL spectra, weakening coupling strength of exciton-LO phonon as decreasing the particle sizes.
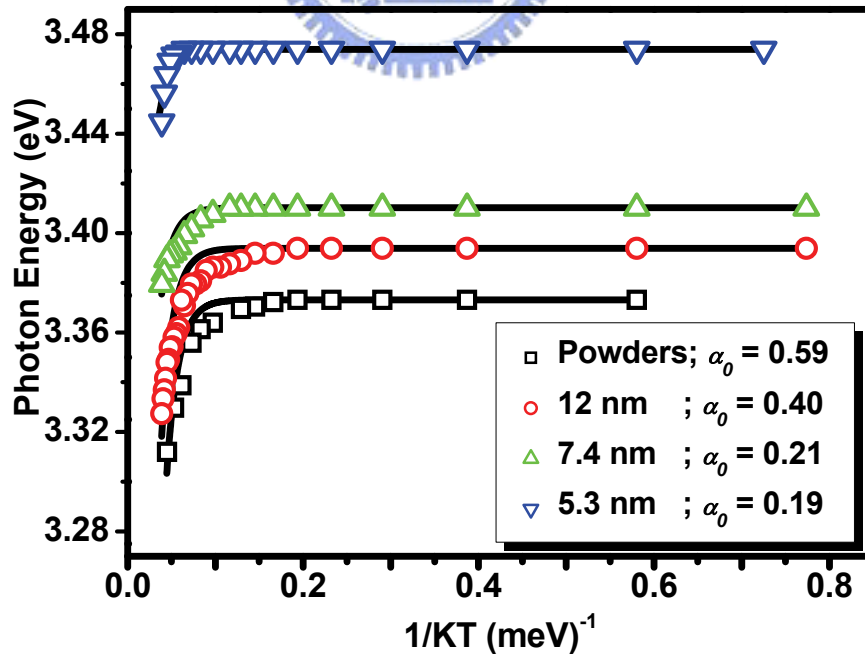

Figure 4-3 Experimental and calculated (solid line) exciton energies plotted against inverse temperature for different ZnO particle sizes.

4.1.4 Binding energy

From the temperature-dependence PL, we can obtain the exciton binding energy (E_b) from the relation (2.25).   The fitting results are shown in Fig. 4-4, E_b of the ZnO powder is 60 meV, which is close to that of ZnO Bulk.   We obtained E_b = 67, 87 and 132 meV, respectively, for 12, 7.4, and 5.3 nm QDs.   The decreasing particle size would raise the electron-hole interaction as a result of the compressing boundary to cause increasing Coulomb energy.   Therefore, the binding energy increases as the particle size decreases.
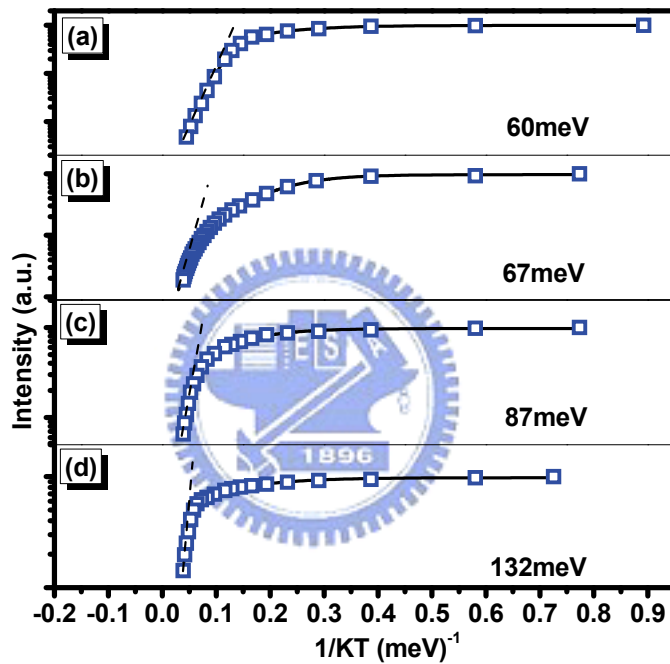
Figure 4-4 The $FX_A^{n=1}$ integral intensity as a function of the inverse temperature from 13 to 300K for (a) Powders, (b) 12nm, (c) 7.4 nm, (d) 5.3 nm.   Squares represent experiment data, while solid lines are the theoretical fitting.

4.1.5 Bohr radius (a_B)

The increasing E_b gives an indication for reduction of exciton-LO phonon interaction. The enhancement of E_b or Coulomb potential indicates a reduction of a_B.   It makes the exciton less polar capable for efficiently interacting with LO-phonon through the Fröhlich interaction.   To find out the relation between a_B and α_0, we calculated a_B from our PL

spectra including the $FX_A^{n=1}$ emission energy and E_b for different dot sizes based on the weak confinement model, Eq. (2.9), and $a_B^2 = \hbar^2/(2\mu^* E_b)$ [28], where $\hbar\omega_0$ is the measured $FX_A^{n=1}$ emission energy plus E_b, $E_g = 3.43$ eV is the band gap energy of bulk ZnO, e is the charge of electron, $\hbar$ is Planck's constant divided by 2π, R is the particle radius, μ^* is the reduced mass of exciton, $\varepsilon = 3.7$ is the relative permittivity [29], and ε_0 is the permittivity of free space. The calculated exciton Bohr radii $a_{B\text{-}QD}$ for 5.3 nm, 7.4 nm and 12 nm QDs are 0.977 nm, 1.038 nm and 1.328 nm. The ratios of $a_{B\,QD}$ to the exciton Bohr radius for bulk ZnO of $a_{B\,bulk} = 2.34$ nm are 0.42, 0.46 and 0.57, respectively, which agree well with 0.42, 0.49 and 0.59 obtained by Senger, et al. [30]

4.1.6   Correlation of α_0 and a_B

Figure 4-5 shows similar trends of $\alpha_{0\,QD}/\alpha_{0\,Powders}$ and $a_{B\,QD}/a_{B\,bulk}$ against the dot size. It represents that the exciton formation is attained by Coulomb interaction, as the particle sizes decrease, the quantum confinement effect causes increase of E_b and decrease of a_B. The electric dipole, which is proportional to the distance of electron-hole pair, is then reduced. The exciton formation thus becomes less polar so that reducing the coupling strength with the polar lattice via the Fröhlich interaction.   Consequently, we demonstrated the reduction of exciton-LO phonon interaction occurs in ZnO-QD system.
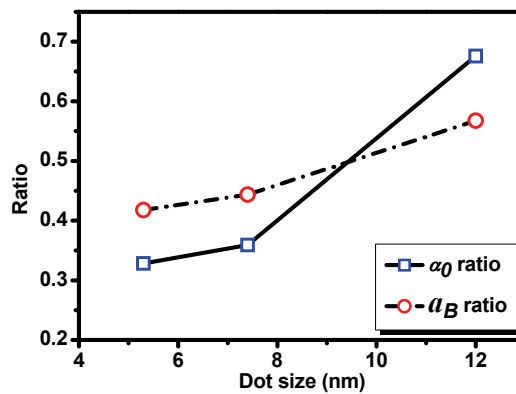

Figure 4-5 The relation of $\alpha_{0\,QD}/\alpha_{0\,Powders}$ and $a_{B\,QD}/a_{B\,Powders}$ with different dot sizes.

4.1.7　　Summary

The temperature-dependent PL of different sizes of ZnO particles showed above unobvious LO-phonon replicas of $FX_A^{n=1}$ in ZnO QDs. The decreasing $FX_A^{n=1}$ emission energy difference of 13-300 K and the increasing exciton binding energy E_b with the decreasing quantum dot size can be obtained from temperature-dependent PL. The deduced α_0 revealed the reduction of exciton-LO phonon interaction. The reduced a_B with particle size obtained from E_b confirms that the exciton becomes less polar in turn reducing the Fröhlich interaction and the exciton-LO phonon interaction is reduced with decreasing ZnO QDs.

4.2　$Mg_xZn_{1-x}O$ alloy system

We have successfully deduced the relation of exciton-LO phonon interaction with shrinking ZnO QDs above. Next, we used the same process to examine the exciton-LO phonon interaction in the $Mg_xZn_{1-x}O$ system
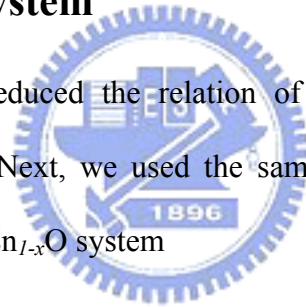
4.2.1　　Morphology and temperature-dependent photoluminescence

The average crystallite sizes of $Mg_xZn_{1-x}O$ and ZnO powders were estimated from the scanning electron microscopy images in Fig. 4-6 and its inset, respectively, to be 1 ± 0.5 μm that does not reveal quantum size effect (Bohr radius of exciton in ZnO is ~2.34 nm [30, 31]). Accordingly, the exciton behavior was affected mainly by the incorporation of Mg. The near band edge (NBE) emissions of the ZnO and $Mg_{0.05}Zn_{0.95}O$ samples measured at various temperatures are shown in Fig. 4-2(a) and 4-7, respectively. First, we discuss the PL spectra of the undoped sample in order to comparatively assign the PL peaks of the $Mg_{0.05}Zn_{0.95}O$ powders. At T = 13 K (Fig. 4-2(a)), the A-free exciton emission (denoted by $FX_A^{n=1}$) is

observed at 3.373 eV.   Besides the broad line at the lower energy shoulder around 3.308 eV labeled as "P", we also found several LO-phonon replicas separated by a constant interval of 71-73 meV.   The P line can be resolved into two-electron satellite [32], donor-to-acceptor pair [33, 34], exciton-exciton scattering [35], and 1LO-phonon replica of $FX_A^{n=1}$ and D^oX, respectively.   With increasing temperature, the relative intensity of $FX_A^{n=1}$ increases whereas that of D^oX decreases and becomes not detectable for T > 80 K.   This is due to the thermal dissociation of bound exciton into free exciton at higher temperature.   As further increasing temperature, the A exciton, and P line finally merge into a broad peak.   At RT, the exciton peak position at ~ 3.309 eV.
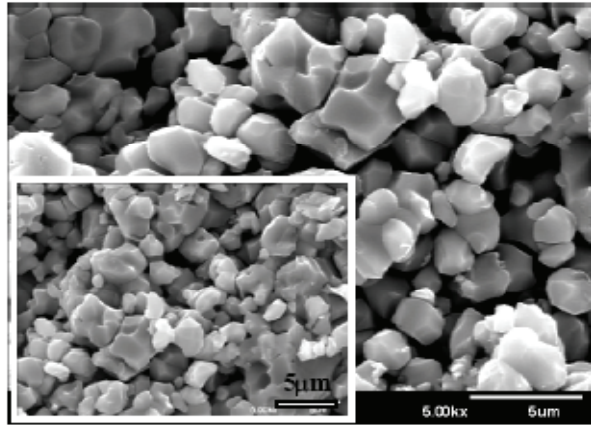

Fig. 4-6 The SEM image of the 5% Mg sample.   The inset shows the pure ZnO powders.

The NBE emission of the $Mg_{0.05}Zn_{0.95}O$ sample was shown in Fig. 4-7; it would evolve from that of the ZnO sample.   According to the opposite temperature dependence of the relative emission intensity, the peaks at 3.422 eV is reasonably assigned to the $FX_A^{n=1}$ transitions.   The NBE peak position at RT exhibits a maximum blueshift of ~ 74 meV as 5 at.% Mg was introduced into the ZnO powders.   Based on the formula: $E(Mg_xZn_{1-x}O) = E(ZnO) + 1.64 * x$ (eV), the Mg content in the $Mg_xZn_{1-x}O$ thin films has been determined for $0 \le x \le 0.2$, grown by PLD [36].   Here, $E(Mg_xZn_{1-x}O)$ and E (ZnO) are the NBE emission

peak positions of $Mg_xZn_{1-x}O$ and ZnO, respectively. The calculated Mg contents of our $Mg_xZn_{1-x}O$ alloys were shown in Table 4-1, e.g., the molar ratio of Mg/Zn = 5% was estimated to be ~ 4.51%. Therefore, the blueshift of the UV emission demonstrated that the Mg ions had incorporated into the ZnO host lattice.
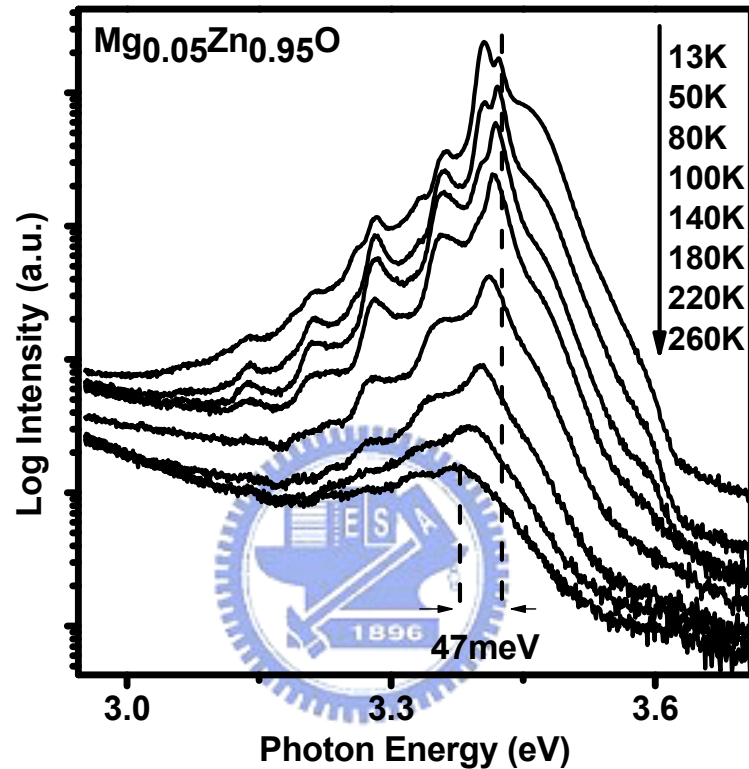
Fig. 4-7 Temperature dependence of PL spectra in $Mg_{0.05}Zn_{0.95}O$ powders. The dashed line marked the peak energies of 13 and 260K

4.2.2   Binding energy

Figures 4-4(a) and 4-8 show the peak intensity of the $FX_A^{n=1}$ emission as a function of reciprocal temperature for the undoped and Mg-doped samples, respectively. The data can be described by Eq. (2.25). The curve fitting gives rise to two binding energies (E_b) of about 60 meV for ZnO powders (Fig. 4-3(a)) and about 73 meV for $Mg_{0.05}Zn_{0.95}O$ powders (Fig. 4-8). Table 4-1 clearly shows that the binding energy of $FX_A^{n=1}$ increases markedly in

samples of higher x.   Therefore, it implies that the exciton localization takes place and that the degree of localization increases with increasing x.   The essential origin of the localization is thought to be the spatial fluctuation of the local composition of Mg in the alloys, which results in the spatial fluctuation of the potential energy for the excitons.
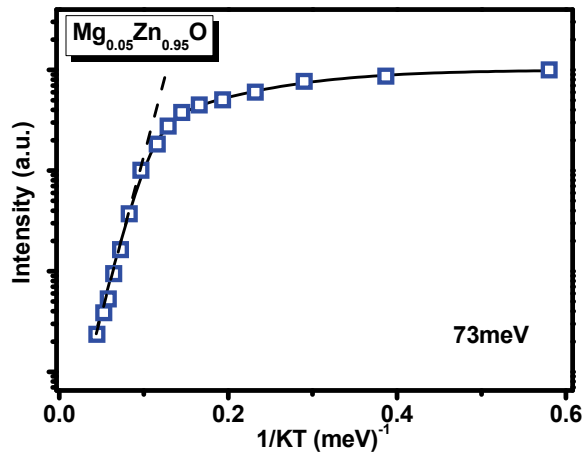

Fig. 4-8 Normalized integrated intensity of ZnO sample as a function of temperature.

4.2.3   The weighting of exciton-LO phonon coupling strength (α_0)

It is well known the increase of E_b may result from the decrease of a_B or effective reduced mass.   Due to the electron is more delocalized than the hole in the bulk exciton, the polar lattice experience a net negative charge in the outer regions of the exciton, while it experiences a net positive one in the inner regions.   This charge inhomogeneity couples to the polar lattice via the Fröhlich mechanism that leads to reduce a_B and to reduce the exciton-LO-phonon coupling.   Thus, we further deduced the coupling strength of free exciton A with LO phonon from temperature-dependent energy shift of $FX_A^{n=1}$ as increasing Mg concentration according to the expression (2.27).   Here $E(0)$ represents the emission energy of free exciton A at $T = 0$ K, $\hbar\omega_{LO} = 72$ meV is the LO phonon energy, and α_{0i} is a proportional weighting which reflects a change in the exciton-LO-phonon interaction. Figure 4-9 depicts the PL-peak energy shift as a function of the temperature with different Mg

concentrations.   Notice that we had set the PL-peak energy position to zero for $Mg_{0.05}Zn_{0.95}O$

powders at 13 K.   By fitting the experimental data for all the $Mg_xZn_{1-x}O$ and ZnO powders

from T = 13 to 260 K with Eq. (2.27), the exciton-LO-phonon coupling of each $Mg_xZn_{1-x}O$

sample are compared with ZnO powder by taking the average ratios, $\alpha_{0\,MgxZn1-xO}/\alpha_{0\,ZnO}$,

which are listed in Table 4-1 clearly show decreasing as more Mg incorporation.   Even

though a_B and α_0 are not directly proportional, there is a relation: If a_B reduces α_0 will also

reduce.   Assuming that the Mg-doped ZnO powders have almost the same effective electron

and hole masses as the undoped ZnO powders due to a small amount of Mg^{2+} substitution for

Zn^{2+}, we calculated a_B from E_b.
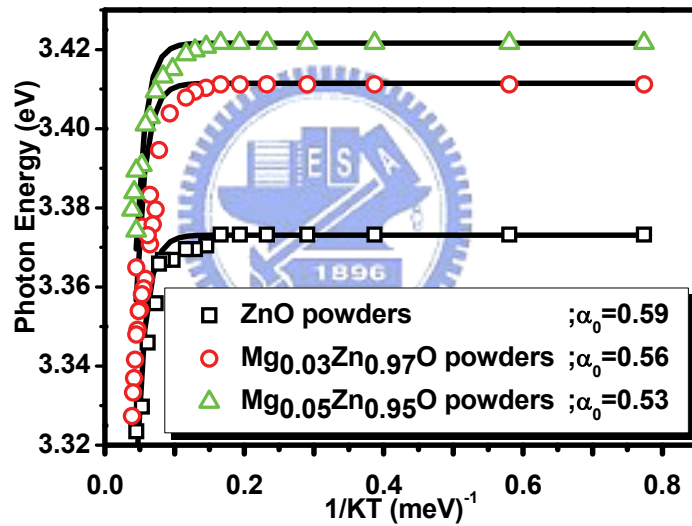
Fig. 4-9 Dependence of PL peak energy positions on temperature for the $Mg_xZn_{1-x}O$ alloys (x = 5%, 3%, and

zero).

4.2.4   Correlation of α_0 and a_B

The correlation between α_0 and a_B normalized to ZnO powders are shown in Fig. 4-10

with open triangles and squares, respectively.   Besides, the solid dots are obtained by the

modified effective masses, which were corrected from MgZnO electronic band structure using

semi-empirical tight-binding approach sp^3 model [37, 38] and virtual-crystal approximation

method [39] done by Mr. Kuo-Feng Lin in our laboratory.   Therefore, a contraction of a_B will make it less polar thereby reducing the coupling to LO phonons.   The results show that relaxation by means of LO phonon becomes less important as the more Mg incorporation. Consequently, we attribute this reducing coupling effect to increase in E_b with raising Mg mole fraction up to 5% of $Mg_xZn_{1-x}O$ powders.   The reduction of $\alpha_{0\,Ex\text{-}LO}$ has to taken into account for the MgZnO-based excitonic device performance in which carrier relaxation to the exciton ground state is a crucial parameter.
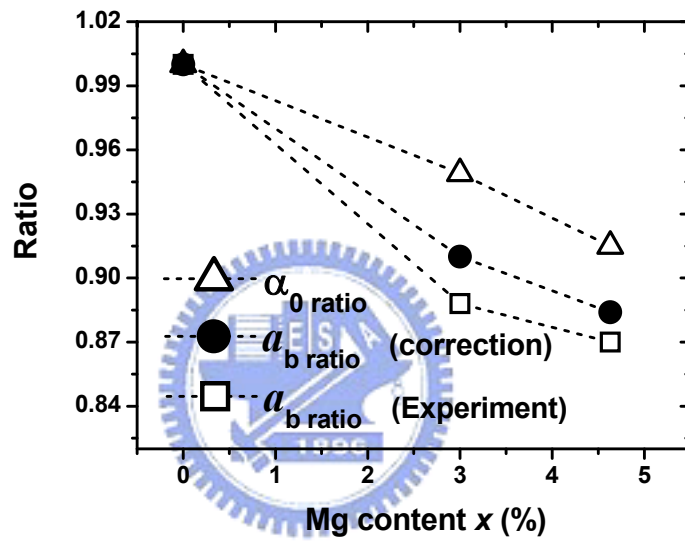

Fig. 4-10 The coupling strength of the exciton-LO-phonon given as the average ratio $\alpha_{0\,ratio} = \alpha_{0\,MgxZn1-xO}/\alpha_{0\,ZnO}$.

For comparison, the diminution of a_b for experiment and correction is also given as $a_{b\,ratio} = a_{b\,MgxZn1-xO}/a_{b\,ZnO}$.

Samples : $Mg_xZn_{1-x}O$	$x=0$	$x=3\%$	$x=5\%$
Calculated Mg content (%)	0	2.9	4.5
Exciton binding energy (eV)	60 ± 4.7	70 ± 6.7	73 ± 8.4
Exciton-LO phonon coupling strength $(\alpha_{0\,MgxZn1-xO}/\alpha_{0\,ZnO})$	1	0.95	0.91

Table 4-1 Summary of the results of the temperature-dependent PL characterization.

4.2.5   Summary

The temperature-dependent NBE PL spectra of $Mg_xZn_{1-x}O$ powders within the range $0 \leq x \leq 0.05$ were measured from 13 K to RT. We deduced experimentally exciton binding energy showing elevation in powders up to 5% Mg substitution. It is suggests that the localization of excitons, because of the compositional fluctuation, takes place in $Mg_xZn_{1-x}O$ alloys and that the degree of the localization increases with increasing x. The reduction of exciton-LO phonon interaction may originate from a diminution in a_B making the exciton less polar, which could be explained by the dopant-induced increase of exciton binding energy.

Chapter 5 Conclusion and perspectives

5.1 Conclusion

We presented temperature-dependent PL of different sizes of ZnO particles and different Mg substitution in $Mg_xZn_{1-x}O$ within the range $0 \leq x \leq 0.05$. The unobvious LO-phonon replicas of the exciton A emission, $FX_A^{n=1}$, were observed when the ZnO particle sizes were under 12 nm in diameter. The $FX_A^{n=1}$ emission energy difference of 13-260 K decreases as the particle size decreases and Mg substitution raises. The increasing exciton binding energy with the decreasing quantum dot size and the increasing Mg content can be obtained from temperature-dependent PL. From the temperature-dependent change of $FX_A^{n=1}$ emission energy, the exciton-LO phonon coupling strength reduces as the particle size decreases and Mg substitution increases. The former is consistent with reducing LO-phonon replica in PL spectra and our previous RRS results [12]. The reduced exciton radius with particle size obtained from exciton binding energy and PL spectra confirms that the exciton becomes less polar in turn reducing the Fröhlich interaction and the exciton-LO phonon interaction is reduced with decreasing ZnO QDs and raising Mg content in $Mg_xZn_{1-x}O$.

5.2 Perspectives

In order to combine the advantages of QDs and Mg-doped ZnO, ZnO-MgO core-shell structure is the most interesting topic for our work. That can overcome the effect of surface defects in ZnO, especially in QDs system which has large surface-volume ratio. Because the band gap energy of MgO is much larger than that of ZnO, the ZnO-MgO core shell QDs should have better emission efficiency than ZnO QDs.

We will also suggest to use simple sol-gel method to add Mg(OAc)$_2$·4H$_2$O in ZnO QDs solution then stir at 40°C.　When the prepared new solution drops on Si then is annealed for 300°C to 700°C.　The primary results of the low temperature PL spectra of samples annealed at various temperatures are shown in Fig. 5-1.　We can observe that a broaden emission from MgZnO alloy and two sharp emission from ZnO.　We also found that the defect emission has been diminished from sample 300°C to 700°C.　To further investigate more characteristic of ZnO-MgO core-shell QDs, the temperature dependent PL and time-resolved PL should proceed.
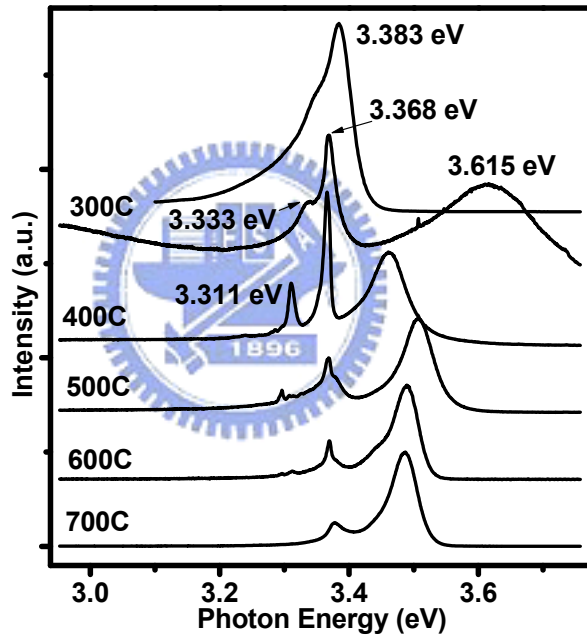

Figure 5-1 PL spectra of different anneal temperatures for ZnO-MgO at 13K.

References

[1] C. R. Ding, S. W. Li , H. Z. Wang, Appl. Phys. Lett. **90**, 241918 (2007).

[2] C. Y. Lee, Y. T. Huang, W. F. Su, and C. F. Lin, Appl. Phys. Lett. **89**, 231116 (2006).

[3] K. Tachibana, T. Someya, Y. Arakawa, R. Werner, A. Forchel, Appl. Phys. Lett. **75**, 2605 (2005).

[4] G. Yusa, H. Sakaki, Superlattices and Microstructures **25**, 247 (1999).

[5] A. Murayama, T. Furuta, K. Hyomi, I. Souma, Y. Oka, D. Dagnelund, I. A. Buyanova, and W. M. Chen, Phys. Rev. B **75**, 195308 (2007).

[6] Y. H. Cho, H. S. Kwack, B. J. Kwon, J. Barjon, J. Brault, B. Daudin, and L. S. Dang, Appl. Phys. Lett. **89**, 251914 (2006).

[7] J. Li, S. H. Wei, S. S. Li, and J. B. Xia, Phys. Rev. B **74**, 081201 (2006).

[8] J. H. Lim, C. K. Kang, K. K. Kim, I. K. Park, D. K. Hwang, and S. J. Park, Adv. Mater. **18**, 2720 (2006).

[9] J. Y. Bae, J. Yoo, and G. C. Yi, Appl. Phys. Lett. **89**, 173114 (2006).

[10] H. Shibata, H. Tampo, K. Matsubara, A. Yamada, K. Sakurai, S. Ishizuka, and S. Niki, and M. Sakai, Appl. Phys. Lett. **90**, 124104 (2007).

[11] P. Ramvall, P. Riblet, S. Nomura, and Y. Aoyagi, J. Appl. Phys. **87**, 3883 (2000).

[12] H. M. Cheng, K. F. Lin, H. C. Hsu, W. F. Hsieh, Appl. Phys. Lett. **88**, 261909 (2006).

[13] R. Chang, and S. H. Lin, Phys. Rev. B **68**, 045326 (2003).

[14] H. D. Sun, T. Makino, Y. Segawa, M. Kawasaki, A. Ohtomo, K. Tamura, and H. Koinuma, Appl. Phys. Lett. **78**, 2464 (2001).

[15] C. J. Brinker and G. W. Scherer, "*Sol-Gel Sience*", p. 303.

[16] C. F. Klingshirn, "*Semiconductor Optics*", p. 169. (1997)

[17] Sun-Bin Yin, "*Fabrication and Characterization of CdS and ZnSe Microcrystalline Doped Glass Thin Films by Pulsed Laser Deposition*", p. 7. National Chiao Tung University Department of Photonics, (1999).

[18] M. A. Stroscio and M. Dutta, "*Phonons in Nanostructures*", p. 41, Cambridge University press, (2005).

[19] C. F. Klingshirn, "*Semiconductor Optics*" , Springer, Berlin, (1997)

[20] A. Teke, U. Ozgur, S. Dogan, X. Gu, and H. Morkoc, Phys. Rev. B, **70**, 195207 (2004).

[21] D. S. Jiang, H. Jung, and K. Ploog, J. Appl. Phys. **64**, 1371 (1988).

[22] G. Ortner, M. Schwab, and M. Bayer, Phys. Rev. B, **72**, 085328 (2005).

[23] C. J. Pan, K. F. Lin, W. T. Hsu, and W. F. Hsieh, Appl. Phys. Lett. **91**, 111907 (2007).

[24] Z. D. Fu, Y. S. Cui, S. Y. Zhang, J. Chen, D. P. Yu, S. L. Zhang, L. Niu and J. Z. Jiang, Appl. Phys. Lett. **90**, 263113 (2007).

[25] V. A. Fonoberov and A. A. Balandin, Appl. Phys. Lett. **85**, 5971 (2004).

[26] C. B. Duke and G. D. Mahan, Phys. Rev. **139**, 1965 (1965).

[27] S. J. Sheih, K. T. Tsen, D. K. Ferry, A. Botchkarev, B. Sverdlov, A. Salvador, and H.

Morkoc, Appl. Phys. Lett. **67**, 1757 (1995).

[28] N. Zettili, Quantum Mechanics, Concepts and Applications (2004).

[29] S.A. Studenikin, N. Golego, M. Cocivera, J. Appl. Phys. **84,** 2287 (1998).

[30] R. T. Senger, and K. K. Bajaj, Phys. Rev. B **68**,045313 (2003).

[31] K. F. Lin, H. M. Cheng, H. C. Hsu, L. J. Lin, and W. F. Hsieh, Chem. Phys. Lett. **409**, 208 (2005).

[32] A. Teke, U. Ozgur, S. Dogan, X. Gu, H. Morkoc, B. Nemeth, J. Nause, and H. O. Everitt, Phys. Rev. B **70**, 195207 (2004).

[33] B. P. Zhang, N. T. Binh, Y. Segawa, K. Wakatsuki, and N. Usami, Appl. Phys. Lett. **83**, 1635 (2003).

[34] B. P. Zhang, N. T. Binh, Y. Segawa, Y. Kashiwaba, and K. Haga, Appl. Phys. Lett. **84**, 586 (2004).

[35] A. Yamamoto, K. Miyajima, T. Goto, H. J. Ko, and T. Yao, J. Appl. Phys. **90**, 4973 (2001).

[36] M. Lorenz, E. M. Kaidashev, A. Rahm, Th. Nobis, J. Lenzner, G. Wagner, D. Spemann, H. Hochmuth, and M. Grundmann, Appl. Phys. Lett. 86, 143113 (2005).

[37] A. Kobayashi, O. F. Sankey, S. M. Volz, and J. D. Dow, Phys. Rev. B **28**, 935 (1983).

[38] K. F. Lin, C. J. Pan, and W. F. Hsieh, submitted to Appl. Phys. Lett.

[39] D. W. Jenkins, and J. D. Dow, Phys. Rev. B **39**, 3317 (1989).